catalysts

MDPI

Article

Crystal-Plane-Dependent Guaiacol Hydrodeoxygenation Performance of Au on Anatase TiO_2

Bin Zhao [1], Xiaoqiang Zhang [2], Jingbo Mao [3], Yanli Wang [1], Guanghui Zhang [1], Zongchao Conrad Zhang [2,*] and Xinwen Guo [1,*]

[1] State Key Laboratory of Fine Chemicals, Frontier Science Center for Smart Materials, PSU-DUT Joint Center for Energy Research, School of Chemical Engineering, Dalian University of Technology, Dalian 116024, China
[2] State Key Laboratory of Catalysis, Dalian National Laboratory for Clean Energy, Dalian Institute of Chemical Physics, Chinese Academy of Sciences, Dalian 116023, China
[3] College of Environmental and Chemical Engineering, Dalian University, Dalian 116622, China
* Correspondence: zczhang@yahoo.com (Z.C.Z.); guoxw@dlut.edu.cn (X.G.)

Abstract: TiO_2-supported catalysts have been widely used for a range of both liquid-phase and gas-phase hydrogenation reactions. However, little is known about the effect of their different crystalline surfaces on their activity during the hydrodeoxygenation process. In this work, Au supported on anatase TiO_2, mainly exposing 101 or 001 facets, was investigated for the hydrodeoxygenation (HDO) of guaiacol. At 300 °C, the strong interaction between the Au and TiO_2-101 surface resulted in the facile reduction of the TiO_2-101 surface with concomitant formation of oxygen vacancies, as shown by the H_2-TPR and H_2-TPD profiles. Meanwhile, the formation of $Au^{\delta-}$, as determined by CO-DRIFT spectra and in situ XPS, was found to promote the demethylation of guaiacol producing methane. However, this strong interaction was absent on the Au/TiO_2-001 catalyst since TiO_2-001 was relatively difficult to be reduced compared with TiO_2-101. The Au on TiO_2-001 just served as the active site for the dissociation of hydrogen without the formation of $Au^{\delta-}$. The hydrogen atoms spilled over to the surface of TiO_2-001 to form a small amount of oxygen vacancies, which resulted in lower activity than that over Au/TiO_2-101. The catalytic activity of the Au/TiO_2 catalyst for hydrodeoxygenation will be controlled by tuning the crystal plane of the TiO_2 support.

Keywords: hydrodeoxygenation; guaiacol; Au/TiO_2; crystal-plane-dependent; $Au^{\delta-}$

check for updates

Citation: Zhao, B.; Zhang, X.; Mao, J.; Wang, Y.; Zhang, G.; Zhang, Z.C.; Guo, X. Crystal-Plane-Dependent Guaiacol Hydrodeoxygenation Performance of Au on Anatase TiO_2. *Catalysts* **2023**, *13*, 699. https://doi.org/10.3390/catal13040699

Academic Editors: Shihui Zou and Juanjuan Liu

Received: 3 March 2023
Revised: 30 March 2023
Accepted: 2 April 2023
Published: 4 April 2023

Copyright: © 2023 by the authors. Licensee MDPI, Basel, Switzerland. This article is an open access article distributed under the terms and conditions of the Creative Commons Attribution (CC BY) license (https://creativecommons.org/licenses/by/4.0/).

1. Introduction

Strong metal-support interactions (SMSI) have been recognized as a common phenomenon in reducible oxide-supported noble metals, and have developed as one of the most important concepts in heterogeneous catalysis [1–4]. Tauster et al. [4] first reported that group VIII metals supported on TiO_2 lost their chemisorption capacity for H_2 and CO after high-temperature reduction. SMSI effects were manifested by the encapsulation of the metal particles [5] and stabilization by supports [6], and by charge transfer between the metal particles and supports [7]. More specifically, Campbell et al. [8] proposed the concept of electronic metal–support interaction (EMSI) via charge transfer between the metal and the support in supported metal catalysts. The SMSI effect can be practically exploited for developing a catalyst by a design strategy considering the chemical bonding and charge transfer at the interface between metal nanoparticles and partially reduced support products to tune the surface electronic and chemical properties of the metal particles [8].

The reducible oxide, TiO_2, usually shows a strong EMSI effect with metal nanoparticles, which can effectively tune the electronic structure of the support metal catalysts, showing better catalytic performance in many catalytic reactions [9,10]. Zhang et al. [11] reported that the different oxidation states of the catalytically active metal sites correlate with different EMSI between the Pt and TiO_2 supports. Highly oxidized Pt clusters demonstrated higher catalytic activity and thermal stability compared with less oxidized Pt clusters. Fu et al. [5]

demonstrated that the electron transfer from TiO_2 to Pt nanoparticles due to the EMSI effect led to the formation of negatively charged Pt. It favored oxygen activation and phenol oxidation. Although TiO_2 is widely reported to tune the electronic properties of the supported metal particles due to EMSI, the origins of the charge transfer on TiO_2 supported metal catalysts remain poorly understood. SMSI between metal and TiO_2 in the hydrodeoxygenation reaction has been widely studied [12,13], but EMSI between them in the hydrodeoxygenation reaction has been less reported.

In our group, TiO_2-supported metal catalysts have been extensively studied due to their excellent catalytic activity and selectivity to phenolics for the HDO of guaiacol [14–17]. A previous study demonstrated Ag supported on reducible TiO_2 exhibited superior activity and selectivity to aromatics for the HDO of guaiacol compared with Ag/SiO_2 or Ag/Al_2O_3. This was attributed to the fact that hydrogen dissociated on the surface of Ag, and then spilled over to and reduced the anatase TiO_2 surface, creating more oxygen vacancies on the Ag/TiO_2-A. These oxygen vacancies were the active sites for the hydrodeoxygenation of guaiacol determined by a linear relationship between the hydrogen consumption for forming oxygen vacancies and the yield of phenols [16]. The evolution of multiple spillover hydrogen species has recently been identified with increasing pre-treatment temperature in H_2 [18]. The oxygen vacancies were found to be filled by hydride species on Ag/TiO_2-A with a very low Ag loading. On Ni/TiO_2-A catalysts, $Ni^{\delta-}$ atoms were found to partially fill in the oxygen vacancies [15]. Mao et al. [17] reported that pure TiO_2-A or Au nanoparticles showed only marginal activity for guaiacol hydrodeoxygenation. However, the Au nanoparticles supported on the surface of TiO_2-A exhibited excellent activity and selectivity to phenolics. The results showed that the easy reduction of TiO_2-A by spillover hydrogen dissociated from the Au nanoparticles facilitated the formation of oxygen vacancies as active sites for HDO of guaiacol.

Intriguingly, little EMSI effect was observed on TiO_2-R (rutile)-supported metal catalysts, which consequently exhibited poor catalytic activity in the hydrodeoxygenation of guaiacol. TiO_2-A has different crystal faces, while the catalytic performance of supported TiO_2-A catalysts in some reactions is dramatically affected by these faces [19–21]. However, several studies have shown an EMSI effect of crystal faces in TiO_2-A on the hydrodeoxygenation of guaiacol. Conceivably, not all the crystal faces in TiO_2-A may contribute equally to the EMSI effect and the catalytic performance. Understanding the differences in the role of the crystal faces in TiO_2-A in the supported catalysts should enable the design of high-performance catalysts for biomass applications. In this work, we report the crystal plane effect of TiO_2-A on the hydrodeoxygenation of guaiacol over Au/TiO_2 catalysts. We synthesized two Au/TiO_2 catalysts exposing different crystal planes of TiO_2 (Au/TiO_2-101 and Au/TiO_2-001). The aim of this work was to study the catalytic performance of Au supported on the different crystal planes of TiO_2 for the HDO of guaiacol, and, further, to understand the fundamental differences between Au/TiO_2-101 and Au/TiO_2-001 catalysts.

2. Results

2.1. Structure Characteristic of TiO_2 and Au/TiO_2

The crystal structure and morphology of the synthesized TiO_2 and Au/TiO_2 catalysts were investigated by XRD, TEM, high-resolution TEM (HRTEM), and BET characterizations. Table 1 summarizes the physical properties of TiO_2 and Au/TiO_2. The BET surface areas of the TiO_2 were both around 110 $m^2 \cdot g^{-1}$. The actual Au contents in the catalysts were close to 1 wt%. The surface areas of the Au catalysts were slightly lower than those of the corresponding supports, This may be have been due to the surface of TiO_2 being occupied by the loaded gold [22].

Table 1. Physical properties of TiO_2 and Au/TiO_2.

Samples	S_{BET} ($m^2 \cdot g^{-1}$)	Au Content (wt%) [a]
TiO_2-101	118	-
TiO_2-001	107	-
Au/TiO_2-101	109	0.91
Au/TiO_2-001	101	1.04

[a] Actual metal loading determined by ICP-AES.

Figure 1 displays the XRD patterns and Raman spectra of the TiO_2 and Au/TiO_2 catalysts exposing different TiO_2 crystal planes. The XRD patterns (Figure 1A) of the as-synthesized catalysts showed the typical diffraction patterns of anatase TiO_2 (JCPDS card no. 21-1272). Obviously, the XRD patterns of TiO_2-101 were the same as the purity anatase TiO_2; however, the intensity of the (004) diffraction peaks of TiO_2-001 was lower and its full width at half-maximum was broadened compared with that of TiO_2-101, indicating that the thickness of the TiO_2 in the 001 direction decreased. In addition, the intensity of the (200) diffraction increased and its full width at half-maximum became narrowed, revealing that the side length of the TiO_2 in the 100 direction increased. The changes in the diffraction peaks of (004) and (200) indicated the formation of TiO_2-001 nanosheets [23]. The anions used in the synthesis were completely removed by washing with NaOH aqueous solution, as shown in XPS (Figure S1, in the Supplementary Materials). No XRD diffraction peak of Au was observed for all the Au/TiO_2 catalysts, indicating the gold of the small nanoparticles was highly dispersed on the surface of TiO_2.

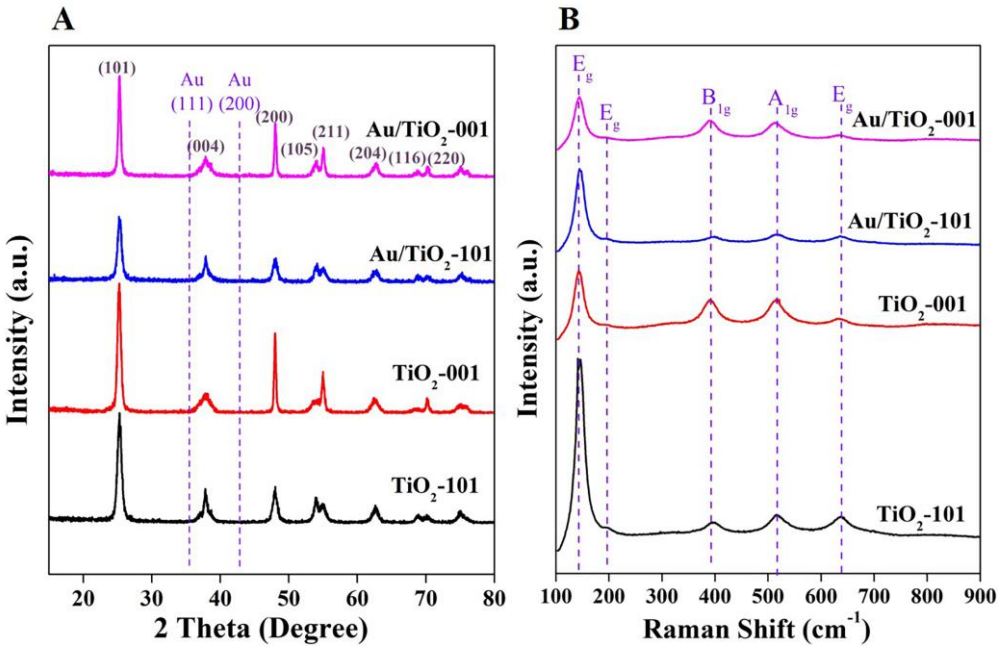


Figure 1. XRD patterns (**A**) and Raman spectra (**B**) of TiO_2-101, Au/TiO_2-101, TiO_2-001 and Au/TiO_2-001.

The Raman spectra (Figure 1B) of the catalysts showed similar bands at 144, 398, 515, and 638 cm^{-1}, which were Raman-active vibrational modes of anatase TiO_2, consistent with the XRD results. The vibrational modes of the E_g peaks at 144 cm^{-1} and 638 cm^{-1} were mainly caused by symmetric stretching vibration of O-Ti-O in TiO_2, the B_{1g} peak at 398 cm^{-1} was caused by the symmetric bending vibration of O-Ti-O, and the A_{1g} peak at 515 cm^{-1} was caused by the antisymmetric bending vibration of O-Ti-O [23]. Compared with TiO_2-101, the distinct intensities of the E_g peaks in TiO_2-001 at 144 and 638 cm^{-1} were lower, while those of the B_{1g} peak at 394 cm^{-1} and the A_{1g} peak at 514 cm^{-1} were higher. This change was consistent with previous reports that the number of the symmetric stretch-

ing vibration modes (E_g) of O-Ti-O on exposed 001 facets in TiO_2 is less than the exposed 101 facets, whereas that of the symmetric bending vibration (A_{1g}) and the antisymmetric bending vibration (B_{1g}) of O-Ti-O is dominant on 001 facets [24].

Figure 2 presents the TEM images of TiO_2-101, Au/TiO_2-101, TiO_2-001 and Au/TiO_2-001 and HRTEM images of Au/TiO_2-101 and Au/TiO_2-001. The morphologies of these nanocrystals were quite uniform. The TiO_2-101 (Figure 2A and Figure S2A, in the Supplementary Materials) nanocrystals possessed a typically octahedral structure, and the size of the nanocrystals was between 30 and 40 nm. The TiO_2-001 (Figure 2B and Figure S2B (in the Supplementary Materials)) was composed of uniform square nanosheets, and the size distribution was 40–60 nm. The lattice fringes resolved in the HRTEM images (Figure S2, in the Supplementary Materials) were about 0.35 nm and 0.24 nm, respectively, which matched with the 101 and 001 crystal planes of anatase TiO_2. These results agree with previously reported results [20,25]. Based on the Wulff construction (Figures S3 and S4, in the Supplementary Materials), we calculated the percentage of each crystal plane in these samples (Table S1, in the Supplementary Materials). The proportion of the 101 or 001 facets was above 80%, indicating that these TiO_2 crystal planes can be used as model supports. The 1 wt% Au/TiO_2 catalysts were prepared by a classic deposition-precipitation method (DP). HRTEM (Figure 2E,F) was used to determine the shape and location of Au nanocrystals. The morphology of Au loaded on the different TiO_2 crystal planes of TiO_2 and the Au nanoparticle size distributions of the Au/TiO_2-101 and Au/TiO_2-001 catalysts are presented in Figure 2C,D. The overall morphology of the Au/TiO_2 samples was comparable to the TiO_2 samples. Tiny particles of Au nanocrystals were well-dispersed on the Au/TiO_2-101 and Au/TiO_2-001 catalysts, as highlighted in the dashed yellow box (Figure 2C,D). The HRTEM images (Figure 2E,F) showed the morphology of the Au nanoparticles and lattice fringes with d = 0.23 nm, consistent with Au (111) [26]. The average particle sizes of the Au nanoparticles was 3.1 $\pm$ 0.5 nm for the Au/TiO_2-101 sample (insert in Figure 2C) and 3.6 $\pm$ 0.5 nm for the Au/TiO_2-001 sample (insert in Figure 2D).

2.2. Chemical Properties of TiO_2 and Au/TiO_2

Figure 3 shows the H_2-TPR profiles of TiO_2-101, TiO_2-001, Au/TiO_2-101 and Au/TiO_2-001. Lv et al. [27] reported that the H_2 molecule desorption temperature on Au surfaces was 276 K for H_2-TPD. However, there was no peak at this temperature, as shown in Figure 4. This indicated that there was no H desorption on Au nanoparticles in this case. The pure TiO_2 supports were barely reducible in the low temperature region, while a significant reduction was observed in the high temperature (HT) region (a peak above 500 °C). The peak c was ascribed to the reduction of TiO_2 in the presence of Au. The interaction between Au and TiO_2 promoted the reduction of TiO_2. For the two Au/TiO_2 catalysts, not only did the high temperature peak shift to low temperature, but a low temperature reduction peak (peak b at about 403 °C) also appeared. The peak b was ascribed to the reduction of Ti^{4+} on the surface of TiO_2 [28], suggesting that the Au interacted with TiO_2 and consequently decreased the reduction temperature of TiO_2. However, a new low temperature reduction peak (peak c at about 221 °C) appeared in the Au/TiO_2-101 catalyst; this peak could be ascribed to the reduction of the surface of TiO_2-101 activated by gold species, forming oxygen vacancies [29]. Shapovalov et al. [30] reported that the bond energy of oxygen on the TiO_2 surface can be weakened in the presence of Au species, implying that, compared with the surface of TiO_2-001, the O atoms on the surface of TiO_2-101 are easier to be removed in the presence of gold species. Moreover, the reducibility of the Au/TiO_2 catalysts below the catalytically relevant temperature of 300 °C followed the order of Au/TiO_2-101 > Au/TiO_2-001, implying a reducibility influence of the exposed crystal plane of the TiO_2 support.

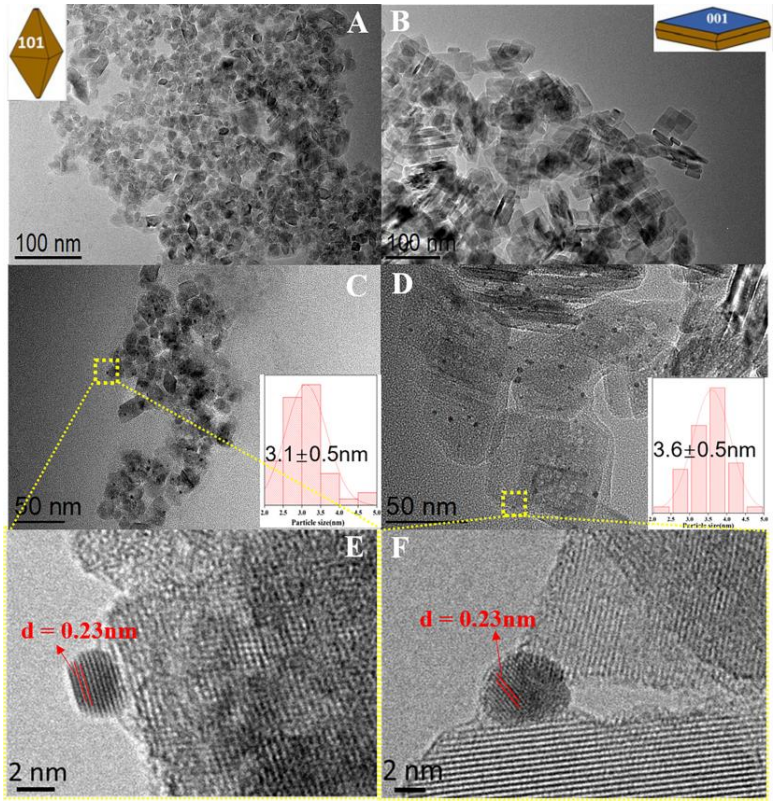


Figure 2. TEM images of TiO_2-101 (**A**), TiO_2-001 (**B**), Au/TiO_2-101 (**C**), Au/TiO_2-001 (**D**) and HRTEM images of Au/TiO_2-101 (**E**) Au/TiO_2-001 (**F**).

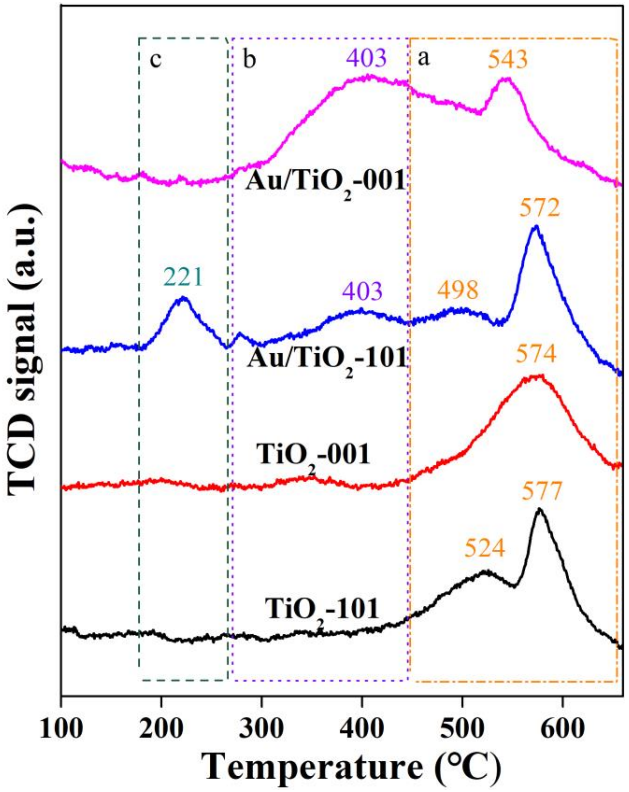


Figure 3. H_2-TPR profiles of TiO_2 and Au/TiO_2 catalysts with different TiO_2 crystal planes. (**a**) the high temperature peak (above 500 °C), (**b**) the medium temperature peak (about 403 °C), (**c**) the low temperature peak (about 221 °C).

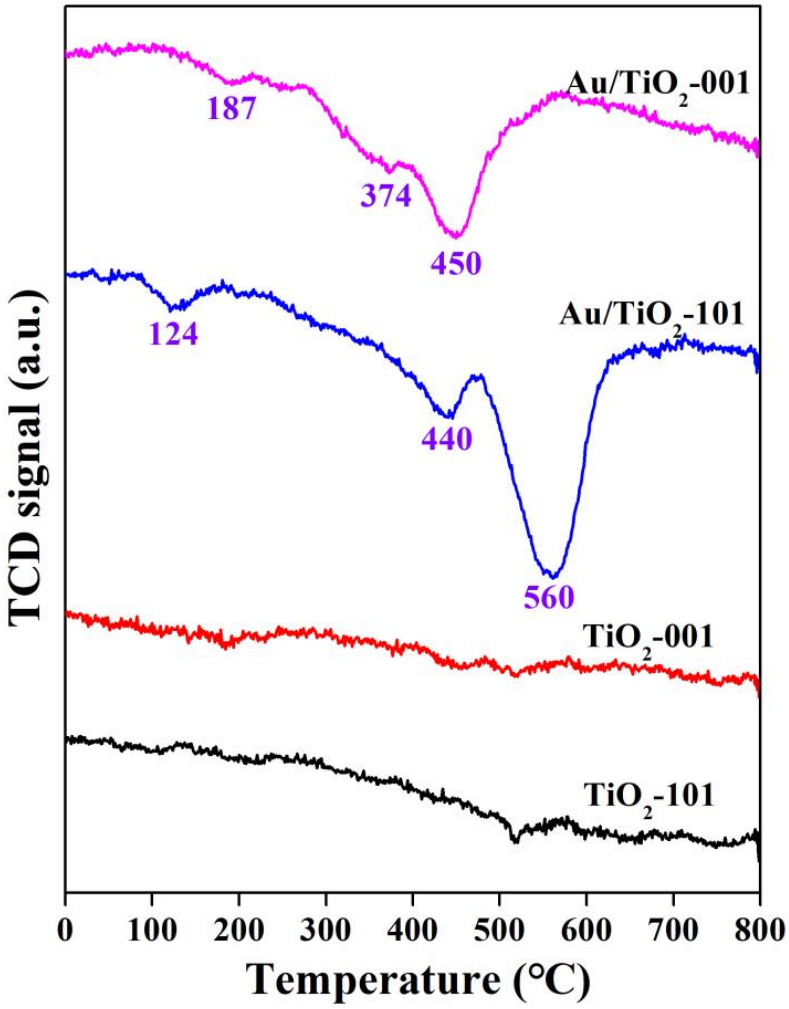


Figure 4. H_2-TPD profiles of TiO_2 and Au/TiO_2 catalysts with different TiO_2 crystal planes.

Figure 4 shows the H_2-TPD profiles of TiO_2-101, TiO_2-001, Au/TiO_2-101 and Au/TiO_2-001. Little hydrogen was desorbed from the pure TiO_2 with different crystal planes. Two desorption peaks can be observed for all the Au/TiO_2 catalysts. The high temperature (about >400 °C) desorption peaks were assigned to spillover hydrogen associated with the TiO_2 [31]. Compared with Au/TiO_2-001, although the temperature of hydrogen desorption of Au/TiO_2-101 was higher, the amount of hydrogen desorption was much larger than that of Au/TiO_2-001. Moreover, a relatively low temperature (<200 °C) desorption peak was detected on the Au/TiO_2-101 catalyst; this was attributed to the desorption of spillover H adsorbed on the oxygen vacancy of the TiO_2 surface [15]. This phenomenon has been reported in previous studies indicating that the spillover hydrogen promoted the reduction of titania on the surface of TiO_2 [16,32,33]. As seen in Figure 4, the temperature of hydrogen desorption of Au/TiO_2-101 was significantly lower than for Au/TiO_2-001, suggesting a less energetically demanding desorption of H_2 on the Au/TiO_2-101 catalyst [34,35]. Hydrogen adsorbed on the oxygen vacancy of the Au/TiO_2-101 surface was more easily desorbed than that on Au/TiO_2-001. On the other hand, the area of desorbed hydrogen on the Au/TiO_2-101 catalyst was much greater than on the Au/TiO_2-001 catalyst, providing further evidence of the reducibility of TiO_2-101 and the strong interaction of Au with this support.

Figure 5 shows the in situ DRIFTS of adsorbed CO on TiO_2-101, TiO_2-001 and two Au/TiO_2 catalysts. As shown in Figure 5 A and B, the CO adsorption peaks at 2173 and 2120 cm^{-1} on the surface of fresh TiO_2 were attributed to physically adsorbed CO. After hydrogen pretreatment, an apparent CO absorption peak located at 2183 cm^{-1} on

TiO_2-101 and TiO_2-001 was observed. This peak can be associated with CO adsorbed on the coordinatively unsaturated Ti^{4+} site (Ti^{4+}-CO) [36–38]. Ulrike Diebold [39] reported that reduced TiO_2 can easily form oxygen vacancies on the surface. The formation of oxygen vacancies occurs at approximately 300 °C or above in a hydrogen atmosphere [40]. Therefore, the unsaturated Ti^{4+} site (Ti^{4+}-CO) was attributed to CO adsorbed on the oxygen vacancy. Obviously, the spectral intensity of TiO_2-101 was much stronger than TiO_2-001, indicating that TiO_2-101 was more easily reduced [41,42]. For Au/TiO_2-001, another new CO absorption peak appeared at 2109 cm^{-1} when Au was supported on the surface of TiO_2-001, which was assigned to the linear adsorption of CO on metallic Au^0 sites based on previous investigations [37,43,44]. Nevertheless, another apparent CO absorption signal was found at 2102 cm^{-1} for Au/TiO_2-101 compared with the v(CO) characteristics of Au/TiO_2-001 at 2109 cm^{-1}. The red shift of CO adsorption on Au/TiO_2-101 indicated that a partial negative state of gold species ($Au^{\delta-}$) was formed on the surface of Au/TiO_2-101 due to the strong metal–support interaction [45]. Moreover, the intensity of CO at 2102 cm^{-1} was higher than that at 2109 cm^{-1} on Au/TiO_2-001, indicating that the $Au^{\delta-}$ on the Au/TiO_2-101 surface showed superior CO adsorption ability.

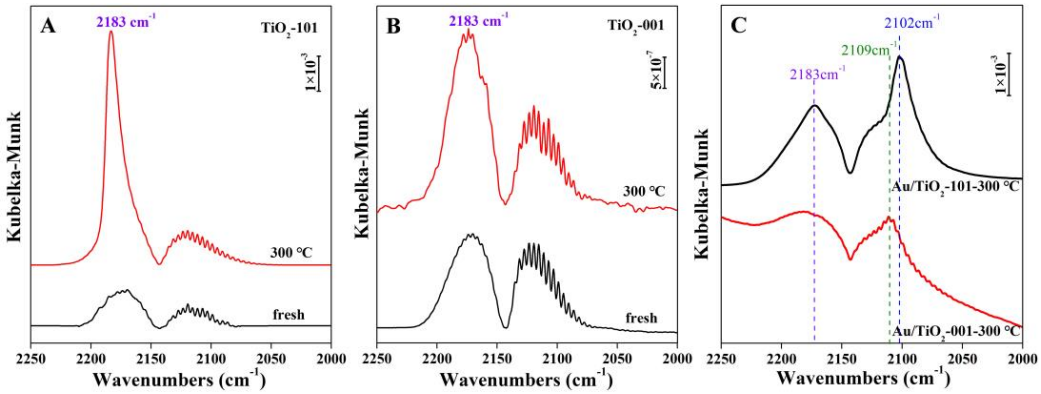


Figure 5. In situ DRIFTS of CO adsorption of TiO_2-101 (**A**), TiO_2-001 (**B**) and Au/TiO_2 catalysts with different TiO_2 crystal planes (**C**).

In order to study the various chemical electronic states of Au, Ti and O species, X-ray photoelectron spectroscopy (XPS) was performed after in situ reduction at 300 °C as a result of the interaction of Au with titania (Figure 6). As shown in Figure 6A, the peaks of Au $4f_{7/2}$ were centered at 83.3 eV on the Au/TiO_2-101 and Au/TiO_2-001, which were very close to the binding energy of metallic Au [43,46]. On the surface of Au/TiO_2-101, another weak signal of 82.3 eV at the 83.3 eV shoulder could be assigned to the presence of electron-rich gold species ($Au^{\delta-}$) [47,48]. The $Au^{\delta-}$ species was found in the DRIFTS of adsorbed CO (Figure 5C). However, this species was not found on the surface of Au/TiO_2-001.

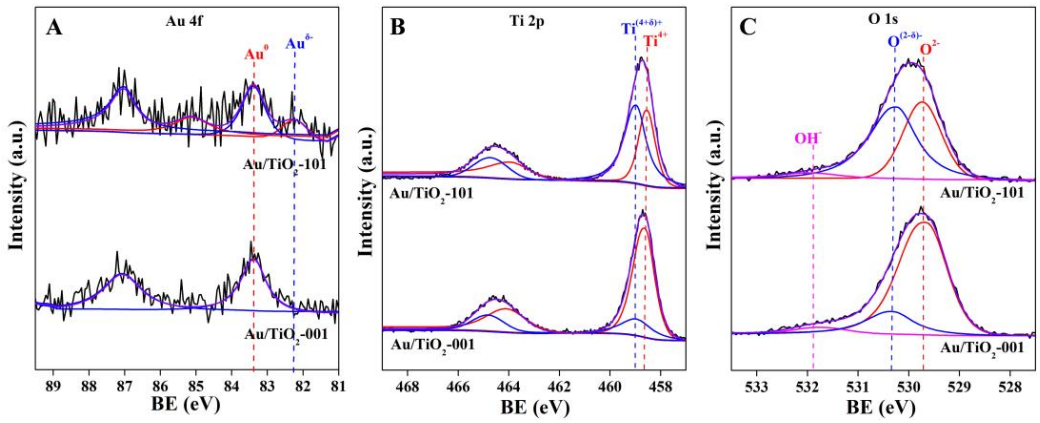


Figure 6. In situ XPS of Au 4f (**A**), Ti 2p (**B**) and O 1s (**C**).

The Ti 2p XPS spectra are shown in Figure 6B. Two binding energies of the Ti $2P_{3/2}$ spectrum at 458.5 and 458.9 eV for Au/TiO_2-101 were observed, assigned to the Ti^{4+} and the more electron-deficient $Ti^{(4+\delta)+}$ species, respectively, according to a previous assignment [49–51]. Radnik et al. [52] reported that the electrons from the carriers were transferred to the gold nanoparticles and accompanied by the formation of negatively charged gold ($Au^{\delta-}$) after hydrogen pretreatment. In this case, the discovery of the $Ti^{(4+\delta)+}$ species can most probably be attributed to electron transfer from the TiO_2 surface to Au, resulting in the loss of electrons of the Ti species on the TiO_2 surface, accompanied by the formation of the $Au^{\delta-}$ species on the TiO_2 surface. The $Au^{\delta-}$ species was found in the XPS of the Au 4f spectra (Figure 6A). Compared with Au/TiO_2-101, the $Au^{\delta-}$ and $Ti^{(4+\delta)+}$ species were also found in the XPS spectrum of the Au/TiO_2-001 sample. However, the Au/TiO_2-001 surface was dominated by Ti^{4+}, while the $Ti^{(4+\delta)+}$ spectral signals were very weak, implying again that the TiO_2-001 surface was difficult to reduce. The DRIFTS of adsorbed CO (Figure 5) and H_2-TPR (Figure 3) also illustrated this phenomenon. The absence of a Ti^{3+} signal in the XPS may have been due to the oxygen vacancies in the filled $Au^{\delta-}$ species or hydride. Taking all the XPS results together, the $Au^{\delta-}$ species and the $Ti^{(4+\delta)+}/O^{(2-\delta)-}$ species were found in the pre-reduced Au/TiO_2-101 catalyst; however, only Au^0 species and Ti^{4+}/O^{2-} species were discovered in the pre-reduced Au/TiO_2-001 catalyst. This suggests that electrons bound to oxygen and titanium ions shifted toward Au atoms occupying the oxygen vacancies. Our group's previous studies [14] demonstrated that adsorbed H on the surface of TiO_2-A formed TiO-H species and Ti-H species for pre-reduced Ni/TiO_2-A.

In addition, XPS spectra (Figure S5, in the Supplementary Materials) in the O 1s region for these two samples were fitted to two peaks at 529.7 and 531.8 eV, attributed to the lattice oxygen (O^{2-}) and adsorbed surface hydroxyl group (OH^-), respectively [46,53–56]. After in situ reduction (Figure 6C), a new binding energy at 530.3 eV was discovered, which was 0.6 eV higher than the O^{2-} species (529.7 eV). Senna et al. [51] reported that the bonding energy of O 1s was shifted to higher energy by co-milling of TiO_2 with poly(tetrafluoroethylene) (PTFE) powder; this shift was caused by the transfer of electrons to adjacent oxygen vacancies. A similar shift was found for Ti species. As shown in the Figure 6C, for Au/TiO_2-101, the binding energy of a large number O^{2-} species (529.7 eV) transferred to higher energy $O^{(2-\delta)-}$ (530.3 eV); simultaneously, the binding energy of many of the Ti^{4+} species at 458.5 eV shifted to $Ti^{(4+\delta)+}$ at 458.9 eV. However, for Au/TiO_2-001, only a small quantity of O^{2-} species shifted to $O^{(2-\delta)-}$. This suggested that it was easier to form the oxygen vacancies on the Au/TiO_2-101 surface than on the Au/TiO_2-001. Combining the in situ XPS of all the elements of Au, Ti and O, it was found that electrons bound to oxygen and titanium ions shifted toward Au atoms, suggesting that the formation of oxygen vacancies was accompanied by the formation of negatively charged Au sites, reflecting the apparent electron metal–support interactions (EMSI) [57].

2.3. Catalytic Performance

TiO_2-101, TiO_2-001 and two Au/TiO_2 catalysts were evaluated by guaiacol HDO to study the effects of TiO_2-101 and TiO_2-001 planes on catalytic performance. The catalyst was pre-reduced at 300 °C before the catalytic reaction took place; however, the morphology of the catalyst did not change before and after the pre-treatment (Figure S6, in the Supplementary Materials). The guaiacol conversion and product distribution are presented in Table 2. First, only phenol was produced as the major product and the C_{8+} product and coke were obviously formed on TiO_2-101 and TiO_2-001 catalysts for guaiacol hydrodeoxygenation at 300 °C. In our previous work [17], we reported that hydrodeoxygenation of guaiacol over Au/AC exhibited marginal activity. The guaiacol conversion was very low on both the two pristine supports. This observation was consistent with our earlier report that TiO_2-A showed low hydrodeoxygenation activity [17]. Second, when Au was supported on TiO_2-101 and TiO_2-001, the guaiacol conversion was much higher over the Au-supported catalysts than that over the TiO_2-101 and TiO_2-001 catalysts. The conversion of guaiacol followed the order:

Au/TiO_2-101 (39.4%) > Au/TiO_2-001 (19.7%) > TiO_2-101 (5.8%) ≈ TiO_2-001 (6.4%). The results demonstrated that the reaction behaviors showed distinct crystal plane dependency. For guaiacol conversion on Au/TiO_2 catalysts, phenol was the primary aromatic product; methylphenol, xylenol, tricresol and catechol were products in small amounts; and cyclohexanol was a byproduct from phenol hydrogenation. The selectivity to phenol followed the order: Au/TiO_2-101 (60.2%) > Au/TiO_2-001 (49.1%) > TiO_2-101 (35.8%) ≈ TiO_2-101 (34.8%). Moreover, the selectivity of phenols increased with decreasing selectivity of the C_{8+} and coke.

Table 2. Conversion and product selectivity for guaiacol hydrodeoxygenation over the various TiO_2 and Au/TiO_2 catalysts [a].

Sample [b]	Conv. (%)	C_6-Ring Sel. (%)					C_1 Sel. (%)	
		Phenol	Catechol	Methylated Phenols	Cyclohexanol	Others [c]	CH_4	CH_3OH
TiO_2-101	5.8	50.1	0	0	0	49.4	-	100
TiO_2-001	6.4	51.6	0	0	0	48.4	-	100
Au/TiO_2-101	39.4	60.2	6.0	23.4	6.5	3.9	80.2	19.8
Au/TiO_2-001	19.7	49.1	9.4	27.7	8.5	5.6	9.4	90.6

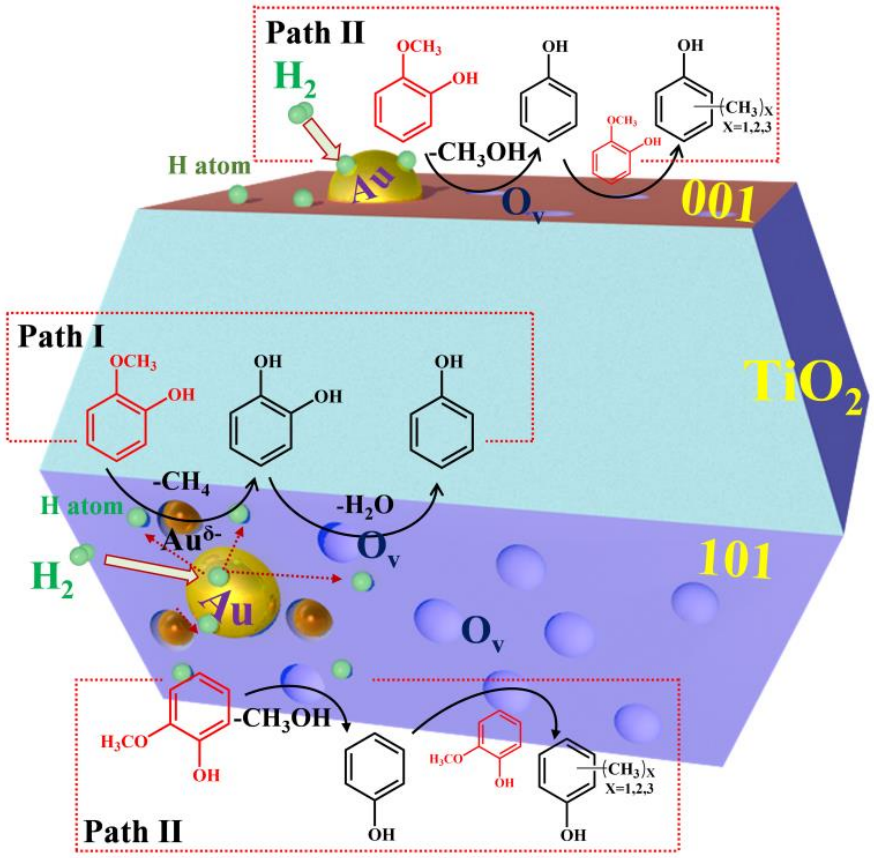
[a] Reaction conditions: guaiacol 1.30 g, catalyst 0.20 g, decane 25 mL, 3 MPa, 700 rpm, 300 °C, 4 h. [b] All the catalysts were pre-treated in 10% H_2/Ar at 300 °C for 1 h before reaction. [c] "Others" in the product yields refer to mostly C_{8+} and coke formed during the reaction testing.

The guaiacol molecule contains three types of C-O bonds: $C_{Ar}O$-CH_3, C_{Ar}-OCH_3, and C_{Ar}-OH, with bond dissociation energies of 262–276, 409–421 and 466 kJ/mol, respectively [58]. It was discovered that the energy barrier of the $C_{aryl}O$-CH_3 bond scission was the lowest, corresponding closely to Au/TiO_2-101 in which the selectivity of methane was much higher than that of methanol (Table 2). Demethylation via cleavage of the Caryl$O$-CH_3 bond was preferential in terms of bond strength compared to demethoxylation by Caryl-OCH_3 bond scission. For instance, sulfide catalysts usually lead to the hydrogenolysis of guaiacol through demethylation forming catechol [59]. In the previous work on Au/TiO_2-A [17], only methanol was formed as the C_1 product during HDO of guaiacol. In contrast, methane was the main C_1 product over a Au/TiO_2-101 catalyst (Table 2). The fact of methanol being formed at a selectivity of 90.6%, together with the small amount of methane in the C_1 product over the Au/TiO_2-001 catalyst, confirmed the different reaction pathway of guaiacol hydrodeoxygenation over the Au/TiO_2-101 catalyst.

In summary, demethylation was much faster than demethoxylation for guaiacol hydrodeoxygenation over the Au/TiO_2-101 catalyst, in contrast to guaiacol hydrodeoxygenation over the Au/TiO_2-001 catalyst, which was possibly due the different properties of Au. The detailed mechanism of guaiacol conversion is discussed below.

2.4. Pathways of Au/TiO$_2$ Catalyst

The different catalytic pathways of the Au/TiO_2-101 and Au/TiO_2-001 catalysts in guaiacol HDO are closely related to the different interactions between Au and TiO_2 with different crystal planes. There are two possible pathways in guaiacol conversion (Scheme 1). No anisole was detected during the HDO process, thus excluding the pathway of guaiacol HDO to form anisole. Methanol was detected as a major C1 by-product (90.6%) over Au/TiO_2-001 (Table 2), indicating that phenol can be obtained directly by the hydrodemethoxylation of guaiacol through path 2. Path 2 is a dominant mechanism in oxygen vacancy [16]. Methylated phenols (cresols, xylenols and trimethylphenols) were also produced. The results confirm the findings of Mao et al. regarding guaiacol HDO on an Au/TiO_2-A catalyst [17].



Scheme 1. Possible pathways in guaiacol hydrodeoxygenation.

On the Au/TiO_2-101 catalyst, catechol and CH_4 were all detected. CH_4 was the dominant C1 by-product (Table 2), suggesting catechol may form through the hydrodemethylation of guaiacol through path 1. The direct hydrodemethylation process of guaiacol occurred mainly on the $Au^{\delta-}$ species. Catechol was further rapidly hydrogenated to phenol, because the rate of catechol HDO is much faster than that of guaiacol [17]. In addition, a small amount of methanol was also detected, implying that the direct demethoxylation of guaiacol may proceed through path 2.

2.5. Stability of Au/TiO_2 Catalyst

The stability of the Au/TiO_2-101 catalyst was investigated by guaiacol hydrogenation testing using the catalyst in three consecutive tests. The HDO conversion of guaiacol and the product selectivity are shown in Figure 7. At the end of the reaction, the catalyst was filtered and recovered without further treatment. It can be seen that there was an insignificant decrease for the guaiacol conversion and product yields in the recycling tests, possibly caused by small losses of catalysts during operation. This suggests that the Au/TiO_2-101 catalyst showed good catalytic stability for the HDO conversion of guaiacol under the investigated conditions.

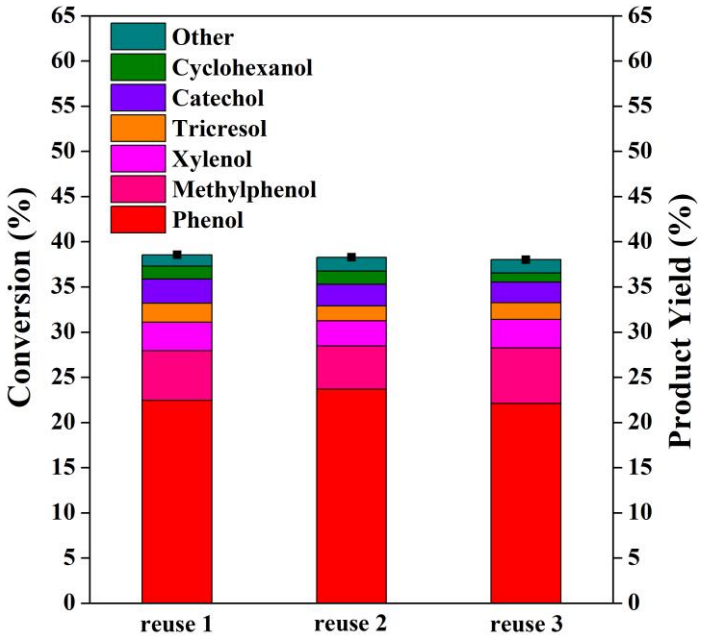


Figure 7. Recycling tests of Au/TiO_2-101. The recycled catalyst was directly used in the next recycling experiments without any treatment.

3. Discussion

As the guaiacol hydrodeoxygenation took place at 300 °C, hydrogen was preferentially dissociated on the Au/TiO_2-101 catalyst under this condition, as shown by H_2-TPD (Figure 4), then spillover occurred to reduce the surface of TiO_2-101 (Figure 3), forming oxygen vacancies. Meanwhile, an EMSI effect and favorable electron transfer from the support to gold caused the formation of negatively charged gold ($Au^{\delta-}$). The DRIFT spectroscopy and in situ XPS demonstrated the presence of the $Au^{\delta-}$ species. Compared with Au/TiO_2-101, the $Au^{\delta-}$ species were not detected on the surface of Au/TiO_2-001. In situ DRIFT spectroscopy demonstrated that the spectral intensity of the Ti^{4+}-CO absorption signal was evidently much higher than for Au/TiO_2-001, indicating a higher concentration of oxygen vacancies on the Au/TiO_2-101 surface than on the Au/TiO_2-001 surface. In situ XPS also demonstrated the binding energy of a large number of O^{2-} species (529.7 eV) transferred to higher energy $O^{(2-\delta)-}$ (530.3 eV) for Au/TiO_2-101, in clear contrast to only a small amount of O^{2-} species shifted to $O^{(2-\delta)-}$ for Au/TiO_2-001. This evidence also confirmed the stronger EMSI effect on the Au/TiO_2-101 surface than on the Au/TiO_2-001 surface. Wang et al. [60] reported that electron-rich Ru species inhibited the ring hydrogenation reaction and the defect sites on TiO_2 promoted the deoxygenation reaction for guaiacol HDO. Zhang et al. [14] demonstrated that $Ni^{\delta-}$ species of Ni/TiO_2-A selectively catalyzed the hydrogenolysis of C–O bonds of guaiacol and that oxygen vacancies broke the ether-oxygen bond of guaiacol. On the Au/TiO_2-101 catalyst, the presence of large amounts of CH_4 (Table 2) suggests possible C-O hydrodemethylation in the guaiacol conversion, which could take place on the $Au^{\delta-}$ site. The deoxygenation of catechol follows as a kinetically facile step [15] However, on the Au/TiO_2-001 catalyst, the presence of large amounts of methanol (Table 2) indicates that the guaiacol hydrodeoxygenation reaction occurred mainly at the oxygen vacancy. Moreover, the higher concentration of oxygen vacancies on the Au/TiO_2-101 surface is beneficial to improved catalytic activity for guaiacol hydrodeoxygenation compared to the Au/TiO_2-001 surface.

4. Materials and Methods

4.1. Synthesis of TiO_2-101

4.1.1. Synthesis of Precursor

For the preparation of the $Ti(OH)_4$ precursor [20], 6.6 mL $TiCl_4$ was added dropwise to 20 mL HCl solution (0.43 mol/L) in an ice bath. After stirring for 30 min, the solution obtained was added dropwise into 50 mL $NH_3 \cdot H_2O$ solution (5.5 wt%) under stirring at room temperature. Afterward, the PH was adjusted to 6–7 with 4 wt% $NH_3 \cdot H_2O$ solution to obtain a white suspension. Then the mixture was stirred continuously for 2 h. The suspension was centrifugated and then the precipitate obtained was washed using water and ethanol until the residual Cl^- was completely removed. Finally, the precipitate was centrifuged and dried at 70 °C for 12 h to obtain the $Ti(OH)_4$ precursor.

4.1.2. Synthesis of TiO_2-101

TiO_2-101 was prepared according to a previously reported method [20]. A quantity of 0.4 g NH_4Cl was added to a mixture of 30 mL of water and 30 mL of isopropyl alcohol under stirring at room temperature. Next, 4.0 g $Ti(OH)_4$ precursor was dispersed into the above mixed solution under stirring for 20 min, and then subject to ultrasound for 10 min. The obtained suspension was then transferred into a 100 mL Teflon-lined autoclave and reacted for 24 h at 180 °C. On completion, the suspension was centrifuged and then the precipitate obtained was washed using 0.1 M NaOH aqueous solution until the residual Cl^- was completely removed. The precipitate was then washed with ultrapure water and ethanol until neutral. Finally, the precipitate was centrifuged and dried at 80 °C for 12 h to obtain TiO_2-101 nanocrystals.

4.2. Synthesis of TiO_2-001

TiO_2-001 was prepared by the hydrothermal method [61]. A quantity of 4 mL HF solution (40 wt%) was added into 25 mL $Ti(OBu)_4$ (TBOT) under stirring for 30 min at room temperature. The mixed solution was then transferred into a 100 mL Teflon-lined autoclave and heated for 24 h at 180 °C. After reaction, the hydrothermal product was centrifuged and washed with 0.1 M NaOH aqueous solution until the residual Cl^- was completely removed. The precipitate was then washed with ultrapure water and ethanol to neutrality. Finally, the white powder was centrifuged and dried at 80 °C for 12 h to obtain TiO_2-001 nanocrystals.

4.3. Preparation of Au/TiO_2 Catalysts

Au/TiO_2 catalysts were prepared by the deposition−precipitation method [62]. A quantity of 1 g TiO_2 powders were dispersed in 50 mL water under stirring for 15 min at room temperature. $(NH_4)_2CO_3$ solution (25 mL, 1 M) was added dropwise into the above suspension under stirring for 15 min to obtain the TiO_2 suspension. Then, the mixed solution of 4.2 mL $HAuCl_4 \cdot 4H_2O$ solution (24.8 mM) and 25 mL water was added dropwise into the TiO_2 suspension. The system was subsequently stirred at room temperature for 1 h; the as-formed slurry was centrifuged and washed with ultrapure water and ethanol. Finally, the precipitate was dried in vacuum for 12 h at 60 °*C*, and calcined in air for 2 h at 300 °C.

4.4. Catalyst Characterization

X-ray diffraction (XRD) measurements were performed using a PANalytical X'Pert Powder X-ray diffractometer (Tokyo, Japan) equipped with a graphite monochromator and Cu Kα radiation. The diffraction data was scanned 2θ from 5° to 80° and collected using a PIXcel 1D detector (Tokyo, Japan).

UV resonance Raman spectroscopy (UV-Raman) with the exciting line of 325 nm was performed using a home-made triple-stage UV-Raman spectrograph with a spectral resolution of 2 cm^{-1} (Jobin Yvon, Paris, France).

Transmission electron microscopy (TEM) images of all samples were taken on a JEM-2100 instrument (FEI Corp. Portland, OR, USA) with an acceleration voltage of 200 kV and high-resolution TEM (HRTEM) images were obtained using a Tecnai F30 HRTEM instrument (FEI Corp. Portland, OR, USA) operated at 300 kV. The sample was dispersed in ethanol and sonicated for 5 min. The suspension was then mounted in a Cu TEM grid. The distributions of Au particle size were established from the measurements of 100 particles in the TEM images.

The surface areas (SBET) of the sample were determined by the Brunauer–Emmett–Teller method using N_2 adsorption at 77.3 K with a Micromeritics ASAP 2020 physical adsorption analyzer (Norcross, GA, USA). The samples were degassed at 280 °C for 5 h prior to the measurements.

Elemental analysis of samples was conducted using a PerkinElmer Optima 8000 inductively coupled plasma-optical emission spectrometer (ICP-OES) (Shanghai, China).

Temperature-programmed reduction in hydrogen (H_2-TPR) experiments were performed using a Micromeritics AutoChem II 2920 chemisorption analyzer (Micromeritics, Norcross, GA, USA). A 100 mg sample was placed in a tubular quartz reactor and heated from room temperature to 750 °C under 10% H_2/Ar at a heating rate of 10 °C/min. H_2 consumption was measured using a thermal conductivity detector (TCD) (Micromeritics, Norcross, GA, USA).

Temperature programmed desorption in hydrogen (H_2-TPD) was carried out on a Micromeritics AutoChem II 2920 chemisorption analyzer (Micromeritics, Norcross, GA, USA). A 300 mg sample was placed in a tubular quartz reactor, and reduced at 300 °C for 1 h, then cooled to −40 °C for 30 min in 10% H_2/Ar. Next, the sample was purged in Ar for 1 h. H_2 desorption was performed by heating to 800 °C (10 °C min^{-1}) in Ar.

In situ DRIFT spectra of CO adsorption on the samples were collected using a Thermo Scientific Nicolet iS50 (Waltham, MA, USA) equipped with an MCT detector and the spectra were obtained as the average of 64 scans at a resolution of 4 cm^{-1}. Prior to testing, the sample was pressed into the in situ reaction cell. For the fresh sample, the high purity He was introduced for 3 min to collect the background spectrum. Then, the gas mixture of 5% CO/He was passed into a reaction cell at 30 °C for 3 min; then the DRIFT spectrum was recorded after the chemisorption of CO. For the pre-treatment, the sample was heated in 10% H_2/Ar at 10 °C/min to 300 °C for 1 h. After treatment, the sample was purged in He and cooled to 30 °C to collect the background spectrum. Subsequently, the sample was then exposed to 5% CO/He at 30 °C for 3 min and the DRIFT spectrum was recorded after the chemisorption of CO.

4.5. Catalyst Activity Measurements

Guaiacol hydrodeoxygenation was performed in a sealed 50 mL stainless-steel batch reactor. Prior to each reaction, the catalyst was pre-reduced at 300 °C in 10% H_2/Ar for 1 h. A quantity of 1.3 g guaiacol and 25 mL decane were added into the reactor and then 0.20 g catalyst was dispersed into the mixed solution. The reactor was purged with N_2 5 times to remove the air and filled with 3 MPa hydrogen. Further, the reactor was heated to 300 °C and held for 4 h under magnetic stirring at 700 rpm. On completion, the reactor was cooled to ambient temperature. A quantity of 25 mL ethanol absolute as solvent and 0.2394 g n-tetradecane as internal standard were added into the reactor. The liquid reactant mixture was identified by GC-MS and qualitatively analyzed by gas chromatography (Agilent 7890A) (Agilent, Santa Clara, CA, USA) with an HP-5 column (30 m × 0.32 mm × 0.25 μm) and a flame ionization detector (FID) (Agilent, Santa Clara, CA, USA).

The conversion of guaiacol ($X_{guaiacol}$%) and the product yield ($Y_{product}$%) were calculated according to the following equations:

$$X_{guaiacol} = \frac{n_{consumed\ guaiacol}}{n_{initial\ guaiacol}} \times 100\% \quad (1)$$

$$Y_{product} = \frac{n_{phenoloc\ compound}}{n_{initial\ guaiacol}} \times 100\% \quad (2)$$

5. Conclusions

In summary, in this work, we synthesized Au supported on TiO_2-101 and TiO_2-001 and found that crystal planes of TiO_2 had a strong effect on guaiacol HDO. The Au/TiO_2-101 catalyst produced a much higher guaiacol conversion than that over the Au/TiO_2-001 catalyst. The H_2-TPR and H_2-TPD profiles showed easier reduction of the TiO-101 surface resulted in more oxygen vacancies. Moreover, in situ XPS and DRIFTS of adsorbed CO demonstrated the formation of electron-rich Au species ($Au^{\delta-}$) due to electron transfer between Au and TiO_2-101 after hydrogen treatment. In contrast, this phenomenon was not found on the Au/TiO_2-001 catalyst. The high activity of the Au/TiO_2-101 catalyst was attributed to the $Au^{\delta-}$ site at the surface due to the strong electronic metal-support interaction. The $Au^{\delta-}$ site was found to promote the demethylation of guaiacol by producing methane. However, the Au on TiO_2-001 dissociated the hydrogen, and the spillover H to the surface of TiO_2-001 resulted preferentially in the generation of small amounts of oxygen vacancies, which served as active sites for the direct hydrodemethoxylation of guaiacol. This work provides an effective strategy to improve the HDO activity of Au/TiO_2 catalysts by tuning the crystal plane of the support.

Supplementary Materials: The following supporting information can be downloaded at: https://www.mdpi.com/article/10.3390/catal13040699/s1, Figure S1: XPS spectrum of Cl 2p and F 1s in the Au/TiO_2-101(A) and Au/TiO_2-001(B); Figure S2: HRTEM images of TiO_2-101(A), TiO_2-001(B); Table S1: The percentages of different crystal planes in the as-prepared TiO_2 nanocrystals were based on geometric calculation; Figure S3: Geometric model of TiO_2-101 nanocrystals; Figure S4: Geometric model of TiO_2-001 nanocrystals; Figure S5: XPS spectrum of Au 4f (A), Ti 2p (B) and O 1s (C) in Au/TiO_2 catalysts before in-situ reduction; Figure S6: TEM images of Au/TiO_2 catalyst before and after pre-treatment. Au/TiO_2-101-before (A), Au/TiO_2-101-after (B), Au/TiO_2-001-before (C) and Au/TiO_2-001-after (D).

Author Contributions: Conceptualization, B.Z., Z.C.Z. and X.G.; methodology, B.Z. and X.Z.; validation, B.Z.; formal analysis, B.Z., X.Z. and J.M.; investigation, B.Z.; resources, B.Z.; data curation, B.Z.; writing—original draft preparation, B.Z.; writing—review and editing, B.Z., X.Z., Y.W., G.Z., Z.C.Z. and X.G; project administration, X.G.; All authors have read and agreed to the published version of the manuscript.

Funding: This work is supported by the Liaoning Revitalization Talent Program (XLYC2008032), Fundamental Research Funds for the Central Universities (DUT22LAB602).

Data Availability Statement: The data are contained within the article.

Conflicts of Interest: The authors declare no conflict of interest.

References

1. Tauster, S.J.; Fung, S.C.; Baker, R.T.; Horsley, J.A. Strong Interactions in Supported-Metal Catalysts. *Science* **1981**, *211*, 1121–1125. [CrossRef]
2. Tauster, S.J. Strong Metal-Support Interactions. *Acc. Chem. Res.* **1987**, *20*, 389–394. [CrossRef]
3. Li, Y.; Zhang, Y.; Qian, K.; Huang, W. Metal-Support Interactions in Metal/Oxide Catalysts and Oxide-Metal Interactions in Oxide/Metal Inverse Catalysts. *ACS Catal.* **2022**, *12*, 1268–1287. [CrossRef]
4. Tauster, S.J.; Fung, S.C.; Garten, R.L. Strong Metal-Support Interactions. Group 8 Noble Metals Supported on TiO_2. *J. Am. Chem. Soc.* **1978**, *100*, 170–175. [CrossRef]
5. Fu, J.; Zhang, X.; Li, H.; Chen, B.; Ye, S.; Zhang, N.; Yu, Z.; Zheng, J.; Chen, B. Enhancing electronic metal support interaction (EMSI) over Pt/TiO_2 for efficient catalytic wet air oxidation of phenol in wastewater. *J. Hazard. Mater.* **2022**, *426*, 128088. [CrossRef]

6. Wang, L.; Zhang, J.; Zhu, Y.; Xu, S.; Wang, C.; Bian, C.; Meng, X.; Xiao, F.S. Strong Metal-Support Interactions Achieved by Hydroxide-to-Oxide Support Transformation for Preparation of Sinter-Resistant Gold Nanoparticle Catalysts. *ACS Catal.* **2017**, *7*, 7461–7465. [CrossRef]
7. Bruix, A.; Rodriguez, J.A.; Ramírez, P.J.; Senanayake, S.D.; Evans, J.; Park, J.B.; Stacchiola, D.; Liu, P.; Hrbek, J.; Illas, F. A New Type of Strong Metal—Support Interaction and the Production of H_2 through the Transformation of Water on Pt/ CeO_2 (111) and Pt/CeO. *J. Am. Chem. Soc.* **2012**, *134*, 8968–8974. [CrossRef]
8. Xiao, S.; Lu, Y.; Li, X.; Xiao, B.Y.; Wu, L.; Song, J.P.; Xiao, Y.X.; Wu, S.M.; Hu, J.; Wang, Y.; et al. Hierarchically Dual-Mesoporous TiO_2 Microspheres for Enhanced Photocatalytic Properties and Lithium Storage. *Chem. Eur. J.* **2018**, *24*, 13246–13252. [CrossRef] [PubMed]
9. Lin, L.Y.; Kavadiya, S.; He, X.; Wang, W.N.; Karakocak, B.B.; Lin, Y.C.; Berezin, M.Y.; Biswas, P. Engineering stable Pt nanoparticles and oxygen vacancies on defective TiO_2 via introducing strong electronic metal-support interaction for efficient CO_2 photoreduction. *Chem. Eng. J.* **2020**, *389*, 123450. [CrossRef]
10. Wang, Y.; Widmann, D.; Behm, R.J. Influence of TiO_2 Bulk Defects on CO Adsorption and CO Oxidation on Au/TiO_2: Electronic Metal-Support Interactions (EMSIs) in Supported Au Catalysts. *ACS Catal.* **2017**, *7*, 2339–2345. [CrossRef]
11. Zhang, L.; Cheng, X.; Zhang, G.; Qiu, W.; He, H.; Chen, G. High active platinum clusters on titanium dioxide supports toward carbon monoxide oxidation. *Appl. Catal. B* **2020**, *266*, 118629. [CrossRef]
12. Huang, R.; Kwon, O.; Lin, C.; Gorte, R.J. The effects of SMSI on m-Cresol hydrodeoxygenation over Pt/Nb_2O_5 and Pt/TiO_2. *J. Catal.* **2021**, *398*, 102–108. [CrossRef]
13. Zhao, X.; Wu, X.; Wang, H.; Han, J.; Ge, Q.; Zhu, X. Effect of Strong Metal-Support Interaction of Pt/TiO_2 on Hydrodeoxygenation of m-Cresol. *ChemistrySelect* **2018**, *3*, 10364–10370. [CrossRef]
14. Zhang, X.; Yan, P.; Zhao, B.; Zhang, Z.C. Identification of electron-rich mononuclear Ni atoms on TiO_2—A distinguished from Ni particles on TiO_2-R in guaiacol hydrodeoxygenation pathways. *Catal. Sci. Technol.* **2021**, *11*, 297–311. [CrossRef]
15. Zhang, X.; Yan, P.; Zhao, B.; Liu, K.; Kung, M.C.; Kung, H.H.; Chen, S.; Zhang, Z.C. Selective Hydrodeoxygenation of Guaiacol to Phenolics by Ni/Anatase TiO_2 Catalyst Formed by Cross-Surface Migration of Ni and TiO_2. *ACS Catal.* **2019**, *9*, 3551–3563. [CrossRef]
16. Liu, K.; Yan, P.; Jiang, H.; Xia, Z.; Xu, Z.; Bai, S.; Zhang, Z.C. Silver initiated hydrogen spillover on anatase TiO_2 creates active sites for selective hydrodeoxygenation of guaiacol. *J. Catal.* **2019**, *369*, 396–404. [CrossRef]
17. Mao, J.; Zhou, J.; Xia, Z.; Wang, Z.; Xu, Z.; Xu, W.; Yan, P.; Liu, K.; Guo, X.; Zhang, Z.C. Anatase TiO_2 Activated by Gold Nanoparticles for Selective Hydrodeoxygenation of Guaiacol to Phenolics. *ACS Catal.* **2017**, *7*, 695–705. [CrossRef]
18. Liu, K.; Hou, G.; Gao, P.; Nie, X.; Bai, S.; Janik, M.J.; Zhang, Z.C. Evolution of multiple spillover hydrogen species on anatase titanium dioxide. *Cell Rep. Phys. Sci.* **2022**, *3*, 101190. [CrossRef]
19. Yu, S.; Lu, Y.; Gao, F.; Dong, L. Study on the crystal plane effect of CuO/TiO_2 catalysts in NH3-SCR reaction. *Catal. Today* **2020**, *339*, 265–273. [CrossRef]
20. Liu, L.; Gu, X.; Cao, Y.; Yao, X.; Zhang, L.; Tang, C.; Gao, F.; Dong, L. Crystal-plane effects on the catalytic properties of Au/TiO_2. *ACS Catal.* **2013**, *3*, 2768–2775. [CrossRef]
21. Wei, T.; Ding, P.; Wang, T.; Liu, L.M.; An, X.; Yu, X. Facet-Regulating Local Coordination of Dual-Atom Cocatalyzed TiO_2 for Photocatalytic Water Splitting. *ACS Catal.* **2021**, *11*, 14669–14676. [CrossRef]
22. Pham, T.N.; Shi, D.; Sooknoi, T.; Resasco, D.E. Aqueous-phase ketonization of acetic acid over Ru/TiO_2/carbon catalysts. *J. Catal.* **2012**, *295*, 169–178. [CrossRef]
23. Tian, F.; Zhang, Y.; Zhang, J.; Pan, C. Raman spectroscopy: A new approach to measure the percentage of anatase TiO_2 exposed (001) facets. *J. Phys. Chem. C* **2012**, *116*, 7515–7519. [CrossRef]
24. Yu, X.; Kim, B.; Kim, Y.K. Highly Enhanced Photoactivity of Anatase TiO_2 Nanocrystals by Controlled Hydrogenation-Induced Surface Defects. *ACS Catal.* **2013**, *3*, 2479–2486. [CrossRef]
25. Chen, S.; Li, D.; Liu, Y.; Huang, W. Morphology-dependent defect structures and photocatalytic performance of hydrogenated anatase TiO_2 nanocrystals. *J. Catal.* **2016**, *341*, 126–135. [CrossRef]
26. Yang, J.; Mou, C.Y. Ordered mesoporous Au/TiO_2 nanospheres for solvent-free visible-light-driven plasmonic oxidative coupling reactions of amines. *Appl. Catal. B* **2018**, *231*, 283–291. [CrossRef]
27. Lv, S.; Liu, X.; Shen, X. A simulated-TPD study of H_2 desorption on metal surfaces. *Surf. Sci.* **2022**, *718*, 122015. [CrossRef]
28. Ousmane, M.; Liotta, L.F.; Di Carlo, G.; Pantaleo, G.; Venezia, A.M.; Deganello, G.; Retailleau, L.; Boreave, A.; Giroir-Fendler, A. Supported Au catalysts for low-temperature abatement of propene and toluene, as model VOCs: Support effect. *Appl. Catal. B* **2011**, *101*, 629–637. [CrossRef]
29. Yu, J.; Wu, G.; Lu, G.; Mao, D.; Guo, Y. Promoting effects of ceria on the catalytic performance of gold supported on TiO_2 for low-temperature CO oxidation. *RSC Adv.* **2014**, *4*, 16985–16991. [CrossRef]
30. Liu, H.; Kozlov, A.I.; Kozlova, A.P.; Shido, T.; Asakura, K.; Iwasawa, Y. Active oxygen species and mechanism for low-temperature CO oxidation reaction on a TiO_2-supported Au catalyst prepared from Au(PPh3)(NO_3) and as-precipitated titanium hydroxide. *J. Catal.* **1999**, *185*, 252–264. [CrossRef]
31. Byun, M.Y.; Kim, Y.E.; Baek, J.H.; Jae, J.; Lee, M.S. Effect of surface properties of TiO_2 on the performance of Pt/TiO_2 catalysts for furfural hydrogenation. *RSC Adv.* **2022**, *12*, 860–868. [CrossRef]

32. Panayotov, D.A.; Burrows, S.P.; Yates, J.T.; Morris, J.R. Mechanistic studies of hydrogen dissociation and spillover on Au/TiO_2: IR spectroscopy of coadsorbed CO and H-donated electrons. *J. Phys. Chem. C* **2011**, *115*, 22400–22408. [CrossRef]
33. Panayotov, D.A.; Yates, J.T. Spectroscopic detection of hydrogen atom spillover from Au nanoparticles supported on TiO_2: Use of conduction band electrons. *J. Phys. Chem. C* **2007**, *111*, 2959–2964. [CrossRef]
34. Yingxin, L.; Jixiang, C.; Jiyan, Z. Effects of the Supports on Activity of Supported Nickel Catalysts for Hydrogenation of m-Dinitrobenzene to m-Phenylenediamine. *Chin. J. Chem. Eng.* **2007**, *15*, 63–67. [CrossRef]
35. Cárdenas-Lizana, F.; Keane, M.A. Gas phase selective hydrogenation over oxide supported Ni-Au. *Phys. Chem. Chem. Phys.* **2015**, *17*, 28088–28095. [CrossRef] [PubMed]
36. Wang, Y.; Widmann, D.; Heenemann, M.; Diemant, T.; Biskupek, J.; Schlögl, R.; Behm, R.J. The role of electronic metal-support interactions and its temperature dependence: CO adsorption and CO oxidation on Au/TiO_2 catalysts in the presence of TiO_2 bulk defects. *J. Catal.* **2017**, *354*, 46–60. [CrossRef]
37. Brudvig, G.W.; Iverson, T.M.; Maghlaoui, K.; Barber, J.; Iwata, S.; Kern, J.; Saenger, W.; Zouni, A.; Biesiadka, J.; Haumann, M.; et al. Spectroscopic Observation of Dual Catalytic Sites During Oxidation of CO on a $AuTiO_2$ Catalyst. *Science* **2011**, *333*, 736–740.
38. Derrouiche, S.; Gravejat, P.; Bianchi, D. Heats of adsorption of linear CO species adsorbed on the Au° and Ti+δ of a 1% Au/TiO_2 catalyst using in situ FTIR spectroscopy under adsorption equilibrium. *J. Am. Chem. Soc.* **2004**, *126*, 13010–13015. [CrossRef]
39. Diebold, U. The surface science of titanium dioxide. *Surf. Sci. Rep.* **2002**, *48*, 53–229. [CrossRef]
40. Pan, X.; Yang, M.Q.; Fu, X.; Zhang, N.; Xu, Y.J. Defective TiO_2 with oxygen vacancies: Synthesis, properties and photocatalytic applications. *Nanoscale* **2013**, *5*, 3601–3614. [CrossRef]
41. Jia, A.; Zhang, Y.; Song, T.; Zhang, Z.; Tang, C.; Hu, Y.; Zheng, W.; Luo, M.; Lu, J.; Huang, W. Crystal-plane effects of anatase TiO_2 on the selective hydrogenation of crotonaldehyde over Ir/TiO_2 catalysts. *J. Catal.* **2021**, *395*, 10–22. [CrossRef]
42. Liu, L.; Gu, X.; Ji, Z.; Zou, W.; Tang, C.; Gao, F.; Dong, L. Anion-assisted synthesis of TiO_2 nanocrystals with tunable crystal forms and crystal facets and their photocatalytic redox activities in organic reactions. *J. Phys. Chem. C* **2013**, *117*, 18578–18587. [CrossRef]
43. Li, Q.; Wu, C.; Wang, K.; Wang, X.; Chen, X.; Dai, W.; Fu, X. Comparison of the catalytic performance of Au/TiO_2 prepared by in situ photodeposition and deposition precipitation methods for CO oxidation at room temperature under visible light irradiation. *Catal. Sci. Technol.* **2022**, *12*, 237–249. [CrossRef]
44. Grunwaldt, J.; Maciejewski, M.; Becker, O.S.; Fabrizioli, P.; Baiker, A. Comparative Study of Au/TiO_2 and Au/ZrO_2 Catalysts for Low-Temperature CO Oxidation. *J. Catal.* **1999**, *469*, 458–469. [CrossRef]
45. Wei, S.; Wang, W.W.; Fu, X.P.; Li, S.Q.; Jia, C.J. The effect of reactants adsorption and products desorption for Au/TiO_2 in catalyzing CO oxidation. *J. Catal.* **2019**, *376*, 134–145. [CrossRef]
46. Liu, N.; Xu, M.; Yang, Y.; Zhang, S.; Zhang, J.; Wang, W.; Zheng, L.; Hong, S.; Wei, M. Auδ–Ov-Ti^{3+} Interfacial Site: Catalytic Active Center toward Low-Temperature Water Gas Shift Reaction. *ACS Catal.* **2019**, *9*, 2707–2717. [CrossRef]
47. Tsunoyama, H.; Ichikuni, N.; Sakurai, H.; Tsukuda, T. Effect of electronic structures of au clusters stabilized by poly(N-vinyl-2-pyrrolidone) on aerobic oxidation catalysis. *J. Am. Chem. Soc.* **2009**, *131*, 7086–7093. [CrossRef] [PubMed]
48. Liu, Z.; Höfft, O.; Gödde, A.S.; Endres, F. In Situ Electrochemical XPS Monitoring of the Formation of Anionic Gold Species by Cathodic Corrosion of a Gold Electrode in an Ionic Liquid. *J. Phys. Chem. C* **2021**, *125*, 26793–26800. [CrossRef]
49. Erdem, B.; Hunsicker, R.A.; Simmons, G.W.; David Sudol, E.; Dimonie, V.L.; El-Aasser, M.S. XPS and FTIR surface characterization of TiO_2 particles used in polymer encapsulation. *Langmuir* **2001**, *17*, 2664–2669. [CrossRef]
50. Zwijnenburg, A.; Goossens, A.; Sloof, W.G.; Craje, M.W.J. XPS and Mo 1 ssbauer Characterization of Au/TiO_2 Propene Epoxidation Catalysts. *J. Phys. Chem. B* **2002**, *106*, 9853–9862. [CrossRef]
51. Senna, M.; Šepelák, V.; Shi, J.; Bauer, B.; Feldhoff, A.; Laporte, V.; Becker, K.D. Introduction of oxygen vacancies and fluorine into TiO_2 nanoparticles by co-milling with PTFE. *J. Solid State Chem.* **2012**, *187*, 51–57. [CrossRef]
52. Mohr, C.; Claus, P. On the origin of binding energy shifts of core levels of supported gold nanoparticles and dependence of pretreatment and material synthesis. *Phys. Chem. Chem. Phys.* **2003**, *5*, 172–177.
53. Chenakin, S.; Kruse, N. Combining XPS and ToF-SIMS for assessing the CO oxidation activity of Au/TiO_2 catalysts. *J. Catal.* **2018**, *358*, 224–236. [CrossRef]
54. McCafferty, E.; Wightman, J.P. Determination of the concentration of surface hydroxyl groups on metal oxide films by a quantitative XPS method. *Surf. Interface Anal.* **1998**, *26*, 549–564. [CrossRef]
55. Kruse, N.; Chenakin, S. XPS characterization of Au/TiO_2 catalysts: Binding energy assessment and irradiation effects. *Appl. Catal. A-Gen.* **2011**, *391*, 367–376. [CrossRef]
56. Xiao, Q.; Wei, S.; Wang, W.W.; Jia, C.J. The Effect of Hydrogenated TiO_2 to the Au/TiO_2 Catalyst in Catalyzing CO Oxidation. *Langmuir* **2021**, *37*, 3270–3280. [CrossRef]
57. Abdel-Mageed, A.M.; Klyushin, A.; Rezvani, A.; Knop-Gericke, A.; Schlögl, R.; Behm, R.J. Negative Charging of Au Nanoparticles during Methanol Synthesis from CO_2/H_2 on a Au/ZnO Catalyst: Insights from Operando IR and Near-Ambient-Pressure XPS and XAS Measurements. *Angew. Chem. Int. Ed.* **2019**, *58*, 10325–10329. [CrossRef]
58. Wang, X.; Arai, M.; Wu, Q.; Zhang, C.; Zhao, F. Hydrodeoxygenation of lignin-derived phenolics-a review on the active sites of supported metal catalysts. *Green Chem.* **2020**, *22*, 8140–8168. [CrossRef]
59. Zhang, X.; Wang, T.; Ma, L.; Zhang, Q.; Yu, Y.; Liu, Q. Characterization and catalytic properties of Ni and NiCu catalysts supported on ZrO_2-SiO_2 for guaiacol hydrodeoxygenation. *Catal. Commun.* **2013**, *33*, 15–19. [CrossRef]

60. Wang, X.; Wu, P.; Wang, Z.; Zhou, L.; Liu, Y.; Cheng, H.; Arai, M.; Zhang, C.; Zhao, F. Chlorine-Modified Ru/TiO_2 Catalyst for Selective Guaiacol Hydrodeoxygenation. *ACS Sustain Chem. Eng.* **2021**, *9*, 3083–3094. [CrossRef]
61. Han, X.; Kuang, Q.; Jin, M.; Xie, Z.; Zheng, L. Synthesis of titania nanosheets with a high percentage of exposed (001) facets and related photocatalytic properties. *J. Am. Chem. Soc.* **2009**, *131*, 3152–3153. [CrossRef] [PubMed]
62. Wan, J.; Chen, W.; Jia, C.; Zheng, L.; Dong, J.; Zheng, X.; Wang, Y.; Yan, W.; Chen, C.; Peng, Q.; et al. Defect Effects on TiO_2 Nanosheets: Stabilizing Single Atomic Site Au and Promoting Catalytic Properties. *Adv. Mater.* **2018**, *30*, 1705369. [CrossRef] [PubMed]

Disclaimer/Publisher's Note: The statements, opinions and data contained in all publications are solely those of the individual author(s) and contributor(s) and not of MDPI and/or the editor(s). MDPI and/or the editor(s) disclaim responsibility for any injury to people or property resulting from any ideas, methods, instructions or products referred to in the content.